

# Morphology and Kinetics of the Isotropic–Nematic Phase Transition in Dispersions of Hard Rods

M. P. B. van Bruggen,<sup>†</sup> J. K. G. Dhont, and H. N. W. Lekkerkerker\*

Van't Hoff laboratory for Physical and Colloid Chemistry, Debye Institute, Utrecht University, Padualaan 8, 3584 CH Utrecht, The Netherlands

Received July 30, 1998; Revised Manuscript Received December 7, 1998

**ABSTRACT:** The time evolution of the isotropic–nematic phase separation in dispersions of sterically stabilized colloidal rods was studied with polarization microscopy and static small angle light scattering (SALS). The rods aspect ratio is 14. In the biphasic region (between the isotropic–nematic transition volume fraction  $\phi_I = 12.1\%$  and the nematic–melting volume fraction  $\phi_N = 35.1\%$ ) a SALS ring develops at a wavevector  $K_{\max}$  which shifts to smaller  $K$  values in time. Increasing the concentration from  $\phi_I$  to  $\phi_N$ , polarization microscopy indicates a crossover from nucleation-and-growth to spinodal decomposition. Nucleation is accompanied by a decrease of the intensity at large  $K$  as  $\sim K^{-4}$ , which is typically found when sharp interfaces have developed in the system. For spinodal decomposition a much less pronounced decrease is observed within the experimental time window. The rate of phase separation was studied by monitoring both the change of the turbidity and the shift of  $K_{\max}$  in time. A maximum rate is found just within the spinodal region.

## 1. Introduction

Onsager showed that liquid crystal phase transitions can be understood on the basis of the interplay between excluded volume and orientational entropy.<sup>1</sup> For an assembly of (very long and thin) hard rods, the free-energy is written as a functional of the orientation distribution function and the number density of rods. One can show that above a threshold concentration denoted as  $\nu^*$  the free-energy functional becomes unstable with respect to arbitrary variations of the orientation distribution function. The concentration  $\nu^*$  is situated deep in the two-phase region where about 80% of the system has become nematic. More recently, Doi and co-workers showed on the basis of the Smoluchowski equation on the two-particle level that for hard rods indeed spinodal decomposition occurs when the concentration of rods becomes higher than  $\nu^*$ .<sup>2</sup>

In the past the phase behavior of systems containing *lyotropic*, charge stabilized rods such as vanadium pentoxide ( $V_2O_5$ )<sup>3</sup> and tobacco mosaic virus (TMV)<sup>4,5</sup> have been studied extensively. In these dispersions one always mentions that phase separation proceeds via nucleation of nematic droplets, often referred to as tactoids. In view of the work of Onsager and Doi, it is however to be expected that in these lyotropic charge stabilized dispersions a spinodal point exists as well. This has never been verified experimentally. On the other hand experimental studies on *thermotropic* liquid crystalline polymers (LCP's), being the counterpart of lyotropic liquid crystals, do give evidence for spinodal decomposition. For example, a recent polarization microscopy study on phase separating binary mixtures of a random coil polymer and a thermotropic LCP convincingly showed that phase separation can proceed via spinodal decomposition when an isotropic system is rapidly brought to high temperature in the fully nematic region of the phase diagram.<sup>6,7</sup> The effect of the LCP

concentration on the phase separation mechanism was however not investigated and nucleation-and-growth has not been identified. This system was used as a model for a linearized Landau–Ginzburg simulation study using a Flory-form of the free energy.<sup>8</sup> The simulations confirm the experimental findings and in addition, a strong coupling between the LCP concentration and the orientational order parameter was found. Russo and co-workers also found evidence for spinodal-like decomposition by examining the late stage of gelling poly( $\gamma$ -benzyl- $\alpha$ ,L-glutamate) (PBLG) solutions, using video optical microscopy.<sup>9</sup>

The aim of this work is to investigate whether one can discern between a concentration region where phase separation proceeds via nucleation and growth, and a concentration region where phase separation takes place via spinodal decomposition in a system of *lyotropic* rodlike particles. The colloidal rods used in this study can be considered as hard rods to good approximation. For this purpose we use a colloidal model system consisting of sterically stabilized rods. The techniques utilized are polarization microscopy and static small angle light scattering. In addition, by studying the turbidity and the dominant length scales developing in the systems as a function of time, information about the concentration dependence of the rate of phase separation is obtained.

This paper is organized as follows. The characterization and properties of the colloidal system are given in section 2. Section 3 summarizes the experimental methods and the results. The results are analyzed and discussed in section 4 and the conclusions are finally collected in section 5.

## 2. System

**2.1. Particle Characteristics.** Rodlike boehmite particles are prepared in an autoclave from an aqueous acidified aluminum–alkoxy solution at 150 °C. For details we refer to ref 10. Subsequently the boehmite rods are grafted with modified polyisobutylene (Shell, SAP 230  $M_w = 1000$ , contour length  $l$  is 4 nm) making

\* Corresponding author.

<sup>†</sup> Present address: Philips Research, Prof. Holstlaan 4, 5656 AA Eindhoven, The Netherlands.

**Table 1. Characteristics of the Boehmite Dispersion**

$\rho$ (g/mL)	$\langle L \rangle$ (nm)	$\langle D \rangle$ (nm)	$L/D$	$(L/D)_{\text{PIB}}$	$[\eta]_0$ ( $([\eta]_{0,\text{th}})$ )	$C_2$	$k_{\text{H}}$	$\phi_{\text{I}}$ (%)	$\phi_{\text{N}}$ (%)
2.11	250	9.4	27	14	22.5 (16.7)	700	1.4	12.1	35.1

the rods dispersible in cyclohexane. The polyisobutylene (PIB) chains are chemically modified with poly-amine anchor groups, each carrying two PIB chains. These anchor groups attach to the surface of the boehmite rods. The grafting procedure is described in ref 11. Since charge will be removed from the boehmite surfaces during the grafting procedure, the polyisobutylene chains must be sufficiently long in order to protect the rods against van der Waals attraction.<sup>12</sup>

The rods used in this study were characterized elsewhere<sup>13</sup> with transmission electron microscopy (Phillips CM10) and elemental analysis. The average length ( $L$ ) and diameter ( $D$ ) as well as the density ( $\rho$ ) of the grafted boehmite rods are summarized in Table 1. The polydispersity of the sterically stabilized rods is 25% in both length and diameter. The volume fraction of rods is corrected for the fact that the PIB chains enclose solvent. When the rods are much longer than the length  $h$  of the PIB chains, the corrected volume fraction is given by

$$\phi = \frac{c}{\rho_{\text{b}}(1+x)} \left( \frac{D+2h}{D} \right)^2 \quad (2.1)$$

where  $c$  is the mass concentration of the PIB-grafted boehmite rods in the dispersion,  $\rho_{\text{b}}$  is the density of the bare boehmite rods (3.0 g/mL<sup>10</sup>), and  $x$  is the mass fraction of PIB to boehmite (typically 0.25<sup>11</sup>).

**2.2. Viscosity.** The volume fraction ( $\phi$ ) dependence of the zero-shear viscosity ( $\eta_0$ ) of the boehmite dispersion in cyclohexane was determined with a Contraves LS40 rheometer, using a Couette geometry. Temperature was fixed at 20 °C. The concentration dependence of the viscosity was measured over a volume fraction range from 0.05% to 1.2%. The intrinsic viscosity at zero shear  $[\eta]_0$ , defined as

$$[\eta]_0 \equiv \lim_{\phi \rightarrow 0} \left[ \frac{\eta_0/\eta_s - 1}{\phi} \right] \quad (2.2)$$

with  $\eta_s$  being the solvent viscosity, was determined by extrapolating the linear part (at  $\phi < 0.5\%$ ) of  $(\eta_0/\eta_s - 1)/\phi$  vs  $\phi$  to  $\phi = 0$ . The results of the viscosity measurements are also given in Table 1. In this table the theoretical value for cylindrical particles as calculated by Brenner<sup>14</sup> is also included. The two-particle interaction term ( $C_2$  in Table 1) is the slope of  $(\eta_0/\eta_s - 1)/\phi$  vs  $\phi$ . This interaction term is commonly written as  $[\eta]_0^2 k_{\text{H}}$ , which defines the Huggins coefficient  $k_{\text{H}}$ . For true hard rods, without taking hydrodynamics fully into account, this coefficient  $k_{\text{H}}$  is 0.4.<sup>15</sup> We note that both  $[\eta]_0$  and  $k_{\text{H}}$  are higher than is predicted by theory. The fact that these rods are grafted with relatively long and flexible polymers leading to a higher energy dissipation at the particle-solvent interface might explain the higher value of  $[\eta]_0$ . Furthermore hydrodynamic interactions should be taken into account. The Huggins coefficient is found to be extremely sensitive to the exact form of the interaction potential. There are experimental indications that attractive as well as repulsive interactions strongly increase  $k_{\text{H}}$ .<sup>16</sup> Owing to this fact, and the fact that the dispersion has a low viscosity up to very high rod concentrations (i.e. higher order terms seem to be

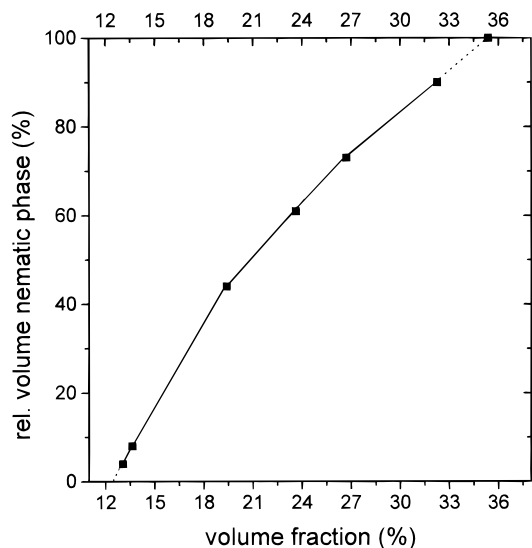


**Figure 1.** Experimental phase diagram of sterically stabilized boehmite rods dispersed in cyclohexane.  $\phi_{\text{I}}$  and  $\phi_{\text{N}}$  are obtained by extrapolating the solid curve (dotted lines).

small), we conclude that these rods can be considered as nearly hard rods.

**2.3. Phase Diagram.** Samples were concentrated by centrifuging a stock-dispersion at 2500 rpm and redispersion of the sediment. Dispersion samples were transferred to rectangular optical cuvettes (Hellma präzisions küvetten) with an optical path of 0.1 cm, and were left equilibrating at a constant temperature of 20 °C. After a few days, the coexisting volumes were measured using a Zeiss Ni-40 cathetometer, connected to an electronic display allowing height measurements with an error as small as 10  $\mu\text{m}$ .

Above a certain threshold concentration the dispersions become turbid in time and separate into a nematic and an isotropic phase. Macroscopic phase separation is complete within 1 or 2 days. At volume fractions above 40% the dispersions become very viscous and difficult to handle. The phase diagram of the dispersion has been determined earlier<sup>13</sup> and could be reproduced albeit that we calculated volume fractions with the use of eq 2.1. The phase diagram is given in Figure 1. The lowest volume fraction at which coexistence is observed, denoted as  $\phi_{\text{I}}$ , is estimated at 12.1% and the volume fraction at which the dispersion has become fully nematic, denoted as  $\phi_{\text{N}}$ , is estimated at 35.1%. The results are also given in Table 1. Onsager theory overestimates the value of  $\phi_{\text{I}}$  in the case of small aspect ratios. Therefore we rely on the simulation results of Bolhuis<sup>17</sup> who mapped out the phase diagram of hard spherocylinders with finite aspect ratios. Here  $\phi_{\text{I}}$  is found to be 18% and  $\phi_{\text{N}}$  to be 22% for  $L/D = 14$ . The fact that the two-phase region in our dispersion is broader can be attributed to polydispersity of the rods.<sup>18,19</sup> The shape of the phase diagram as found for this dispersion resembles the phase diagram of a bidisperse system with a length ratio of 2.5 where the fraction of short rods is 20%. For this system the width of the coexistence region expressed as  $\phi_{\text{N}}/\phi_{\text{I}}$  is as large as 3.5.<sup>20</sup>

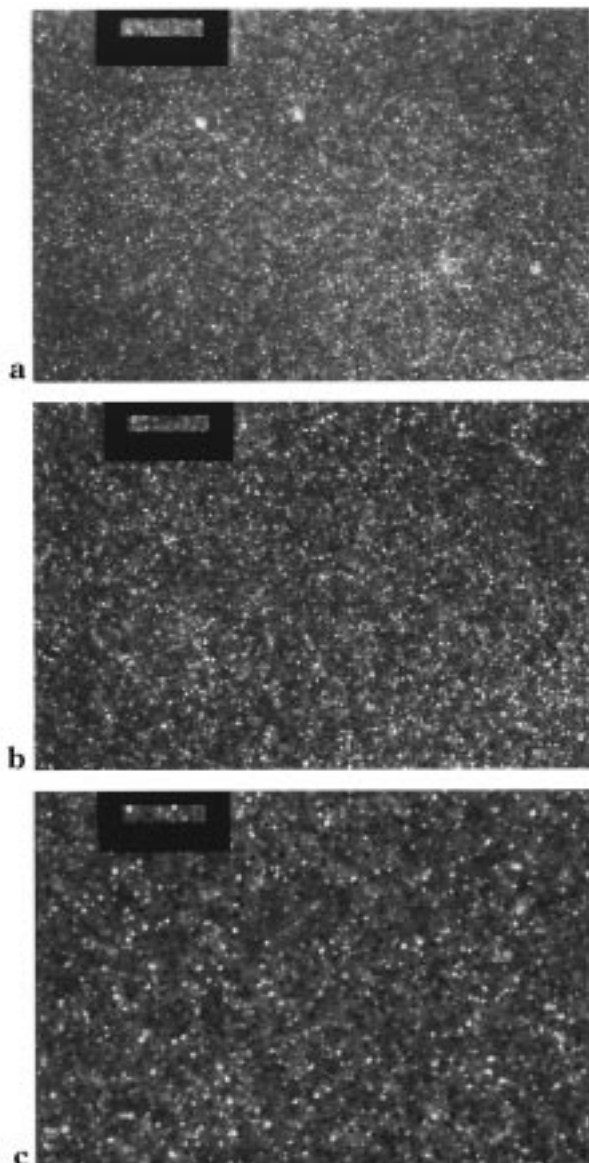


**Figure 2.** Morphological development of a dispersion with an overall concentration of 12.5%, as seen through the polarization microscope after (a) 10 min, (b) 20 min, and (c) 60 min. The bars represent 100  $\mu\text{m}$ .

### 3. Measurements and Results

**3.1. Polarization Microscopy.** The phase separation process was followed under a polarization microscope (Zeiss axioplan microscope). Samples of the dispersions were transferred into 100  $\mu\text{m}$  cuvettes (VitroDynamics) which were quickly sealed, preventing evaporation of the volatile cyclohexane. Immediately after preparation the cuvettes were examined under the polarization microscope.

Two samples which are representative for the two different paths along which phase separation proceeds, were chosen for further investigation. The first system is just in the two phase region at  $\phi = 12.5\%$ , while the second system is more deep in the two-phase region at  $\phi = 20\%$ . The time evolution of the dispersion morphology is shown in Figures 2 and 3. At 12.5%, the sample is initially dark, but after some time, small discrete nuclei become visible to the eye (Figure 2). These droplets grow in time while the number density of droplets decreases. The birefringent nuclei appear as

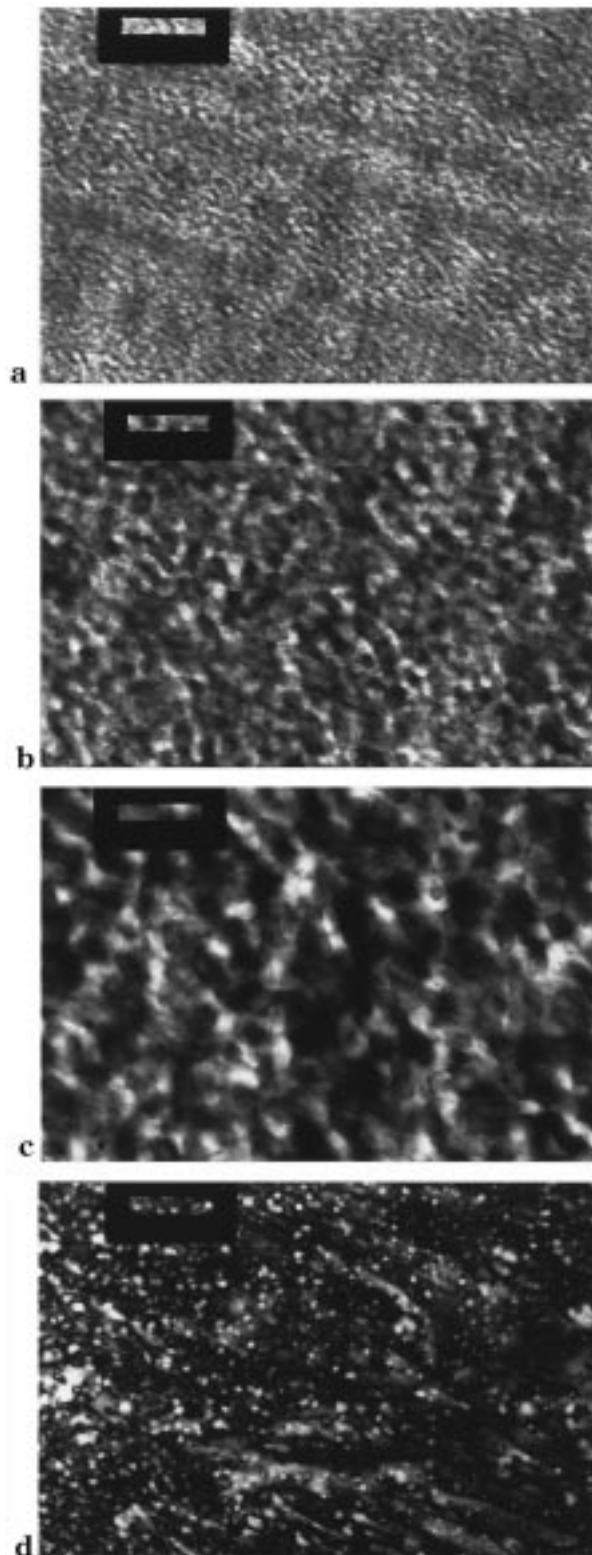


**Figure 3.** Morphological development of a dispersion with an overall concentration of 20%, as seen through the polarization microscope after (a) 5 min, (b) 8 min, and (c) 15 min and (d) 3 h after homogenization. The bars represent 100  $\mu\text{m}$  for parts a–c and 200  $\mu\text{m}$  for part d.

bright or dark, depending on the orientation of the rods inside the nuclei. When the rods are parallel to either the analyzer or polarizer, there is no birefringence and the nucleus is dark; otherwise, birefringence allows the light to be transmitted. At a volume fraction of 20% (Figure 3) initially birefringent regions are visible. The

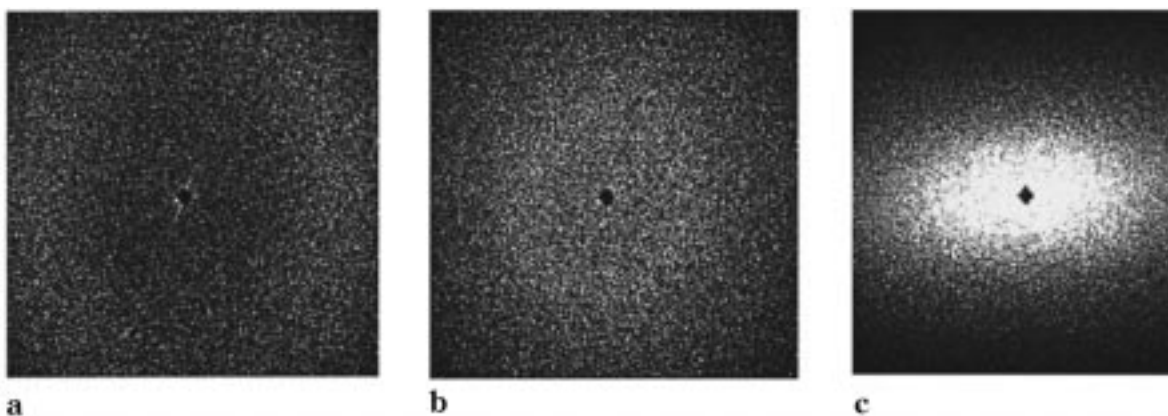


**Figure 4.** Scattered intensities in a 22% sample as detected by the CCD camera after (a) 0 s, (b) 60 s, and (c) 65 min.

interconnected labyrinth structure roughens in time. Eventually, as shown in the last graph in Figure 3, after a few hours this interconnected labyrinth structure transforms to a structure of isolated droplets. Phase-separating dispersions with concentrations higher than 20% exhibited the same spinodal features. Between 12.5% and 20% a crossover between nucleation type and spinodal type of separation was observed; however, this was not investigated in further detail.

### 3.2. Static Small-Angle Light Scattering (SALS).

The SALS setup used in this study is the same as described in refs 21 and 22. A 5 mW randomly polarized helium–neon laser with a wavelength of 632.8 nm was used as the light source which illuminated the 0.1 cm path length rectangular cuvette. The scattered light was projected on a translucent screen which was recorded by a  $165 \times 192$  pixels CCD camera, using an exposure time of 100 ms. The transmitted light intensity was monitored with a photodiode which was positioned behind the screen. Scattering angles, after being corrected for refraction at the edge of the cuvette, ranged from 200 to  $3000 \text{ mm}^{-1}$ , corresponding to scattering angles of  $0.4\text{--}12^\circ$ . All scattering data were radially averaged with an angular resolution of about  $0.07^\circ$ . No background images were subtracted. Concentration quenches were made by vortexing supersaturated dispersions for at least 30 s as turbulent as possible so that shear-induced alignment of the rods was reduced to a minimum. Samples which were not isotropic after vortexing were recognized as such by asymmetric (ellipse-shaped) scattering patterns that appeared on the translucent screen. Figure 4 is a typical example of the scattered intensity in a 22% sample. Immediately after homogenization, a SALS ring appears which becomes more intense, and its radius decreases in time. At the lowest concentrations the ring does not immediately become visible. In time, scattering at the inner side of the ring increases as well so that finally a light-scattering cone remains. In the late stage of the phase-separation process, this cone becomes asymmetric, as can be clearly seen in Figure 4 after 65 min. The deformation is due to sedimentation of the higher density nematic domains which become elongated in the direction of gravity (vertically downwards in Figure 4). This gives rise to a horizontal, ellipse-shaped scattering pattern. Data recording was stopped long before gravitational effects became noticeable because the SALS ring fills up much more rapidly. The scattering data after radial averaging are shown for  $\phi = 12.5\%$  and  $\phi = 20\%$  in Figure 5. Although under the polarization microscope the phase-separation mechanisms seem to

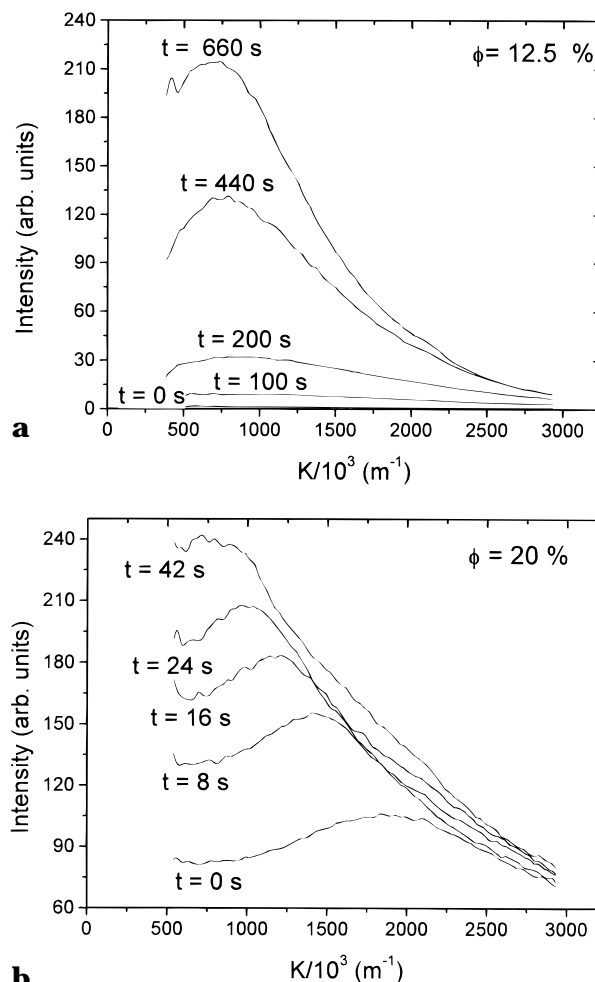


**Figure 5.** Time evolution of the small angle scattering pattern after radial averaging for two different concentrations.

proceed along two different ways, the light-scattering patterns after radial averaging appear quite similar on first sight. Furthermore, it should be mentioned that, with polarization microscopy, changes of the dispersion morphology become visible to the eye after times where the SALS scattering ring has already completely collapsed. So SALS yields information about the *earlier* stages of the phase separation process as compared to polarization microscopy observations. As phase separation proceeds, density inhomogeneities become larger and the turbidity of the demixing dispersion increases. The turbidity  $\tau$  is defined as

$$\tau = d^{-1} \ln \left( \frac{I_0}{I_t} \right) \quad (3.1)$$

with  $d$  the thickness of the cuvette,  $I_0$  the incident intensity, and  $I_t$  the transmitted intensity. In Figure 6 the time evolution of the turbidity is given for a large range of concentrations in the biphasic region. At a concentration of 12.5% where the formation of isolated nuclei is observed under the microscope, the turbidity increases only marginally. Closer inspection of this curve reveals that the turbidity is already increasing at  $t = 0$ . In the 20% system the turbidity increases sharply. So no latency time is measured at any concentration. Apparently, phase separation is triggered within a few seconds in the samples. The fact that at  $t = 0$  the turbidity is not the same for all samples is due to the fact that the increase of the turbidity is strongly concentration dependent; between homogenization of the samples and the actual start of the measurements, the turbidity has raised to different levels.

#### 4. Analysis and Discussion

**4.1. Morphology.** From the morphological changes during the phase-separation process as depicted in Figures 2 and 3, it is concluded that the isotropic–nematic phase separation can either proceed by nucleation and growth or by spinodal decomposition. Both mechanisms give rise to a small-angle light-scattering ring. Often, a small-angle light-scattering ring is interpreted as a typical spinodal feature. The fact that at low as well as at higher concentrations a light-scattering ring is observed does clearly *not* imply that the mechanisms of phase separation are spinodal. In nucleating systems the typical length scale arises from nuclei which are surrounded by a depletion zones with a local density which is lower than the bulk density.<sup>23</sup> As the nuclei grow and the depletion zone becomes more extended, the maximum of the scattered light shifts to smaller angles. Indeed, the crystallization of colloidal spheres has been studied with SALS in this way.<sup>24</sup> A feature which distinguishes nucleation and growth from spinodal decomposition is the induction or latency time that is encountered in nucleating systems.<sup>25,26</sup> During spinodal decomposition this induction time is absent since density fluctuations with arbitrary small amplitudes induced by the Brownian motion of the particles trigger the decomposition process. For nucleating systems density fluctuations which trigger phase separation must exceed a certain minimum amplitude in order to overcome the free-energy nucleation barrier. In crystallizing dispersions of colloidal spheres, induction times can become as long as 1–2 min.<sup>26</sup> Nevertheless, in the concentration range where nucleation is observed in our system, the turbidity of the system immediately increases after homogenization of the sample, indicating that the induction time, when it is present at all, is very short. The reason the induction time is so short might be intrinsically connected to the isotropic–nematic phase separation of rodlike particles. Another reason for the observation of a short induction time may be that during homogenization of the samples, small local orientational correlations are induced, although homogenization was performed as turbulent as possible. These local orientational correlations can act as seeds which start growing immediately when homogenization is stopped.

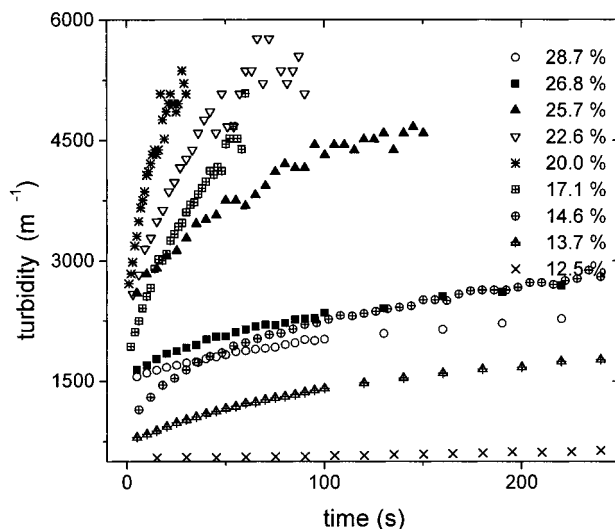


**Figure 6.** Time evolution of the turbidity for concentrations ranging from  $\phi_I$  to  $\phi_N$ .

The first most straightforward attempt to scale the SALS data is by plotting  $I/I_{\max}$  vs  $K/K_{\max}$ , with  $I_{\max}$  the maximum scattered intensity which is measured at a corresponding wave vector  $K_{\max}$ , where  $K$  is equal to

$$K = \frac{4\pi n}{\lambda} \sin\left(\frac{\theta}{2}\right) \quad (4.1)$$

with  $n$  the refractive index of the solvent,  $\lambda$  the wavelength of the laser light in a vacuum, and  $\theta$  the scattering angle. Two different scaling functions are considered here. One is the scaling function proposed by Dhont who derived it from the Smoluchowski equation:<sup>27</sup>

$$\frac{I(K)}{I_{\max}} = \exp \left[ -30 \left( \frac{K}{K_{\max}} - 1 \right)^2 - 25 \left( \frac{K}{K_{\max}} - 1 \right)^3 \right] \quad (4.2)$$

This scaling function is supposed to be valid in the intermediate stage of spinodal decomposition. The other curve is the (off-critical) empirical Furukawa scaling function:<sup>28</sup>

$$\frac{I(K)}{I_{\max}} = \frac{3(K/K_{\max})^2}{2 + (K/K_{\max})^6} \quad (4.3)$$

The Furukawa scaling function is applicable in the late stage of spinodal decomposition where the initial diffuse interfaces between low and high density regions have sharpened. Both equations given here involve the intensity instead of the structure factor because at these small scattering angles the form factor of the rods is very close to unity. Note that both scaling functions are derived for spherical particles where only the local density changes in time. It is not clear whether these scaling functions apply in the case of liquid-crystal phase transitions. Nevertheless, Russo and co-workers<sup>9</sup> found that the Furukawa scaling function did describe their data on gelling solutions of rodlike PBLG. It is not certain whether this gelling was the precursor of a fluid–fluid or an isotropic–nematic phase separation. Schätzel and Ackerson<sup>24</sup> found that the Furukawa scaling function did not describe their SALS data on crystallizing colloidal spheres. Instead they proposed an empirical scaling in which  $I(K)$  is normalized on  $I(K =$

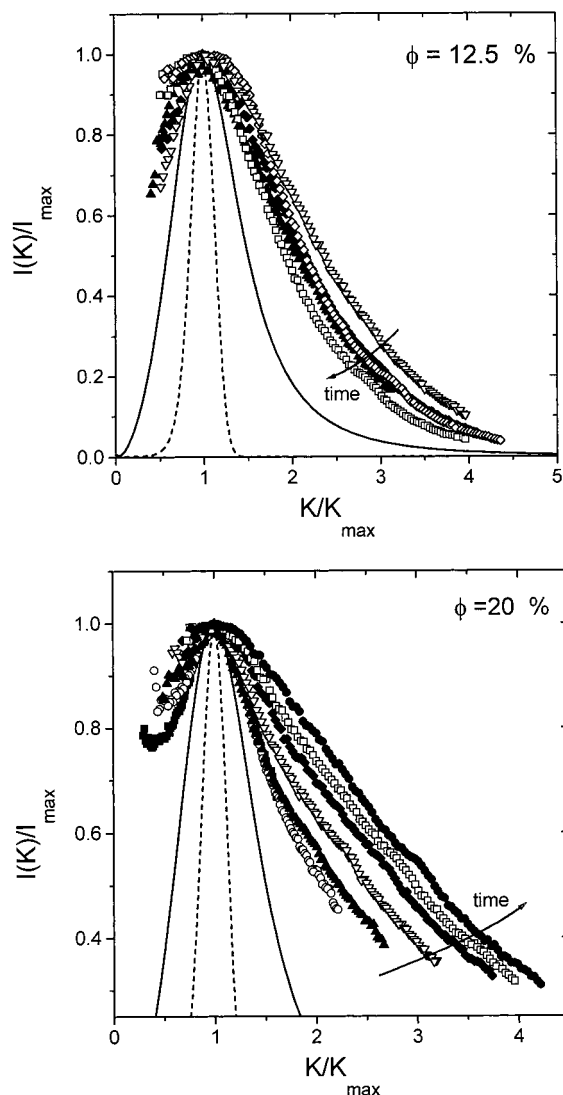


**Figure 7.** SALS data as given in Figure 5, scaled on  $I_{\max}$  and  $K_{\max}$ . The broken (---) curve is scaling curve as given by Dhont<sup>27</sup> for spinodal decomposition in the intermediate stage in systems consisting of spherical particles. The full (—) curve is the Furukawa scaling curve<sup>28</sup> for spinodal decomposition in later stages in systems consisting of spherical particles.

$K_{1/2}$ ), with  $K_{1/2}$  the wave vector at which the scattered intensity has become half of  $I_{\max}$ . Figure 7 demonstrates that scaling of the data does not lead to a satisfactory master curve. In addition both scaling functions are narrower. The scaled data show that in the spinodal region the high  $K$  tails of the scattering curves shift toward *higher*  $K$  values, whereas in the nucleation-and-growth region the high  $K$  tails shift toward *lower*  $K$  values. So at 12.5% a sharpening of length scale is taking place. At 20% the relative occurrence of other length scales is increasing in time. The Furukawa function is a late stage scaling function, implying that concentration gradients have become large and sharp interfaces between high and low density are existing in the system. The Furukawa scaling function reveals that at  $K$  values larger than  $K_{\max}$ , the decrease of the scattered intensity scales as  $K^{-4}$ . According to Porod this dependency is caused by scattering arising from these sharp interfaces.<sup>29</sup> To test whether  $K^{-\beta}$  behavior with  $\beta = 4$  occurs in these systems the large  $K$  regime in Figure 7 is given in a log-log representation in Figure 8. At 12.5% the exponent varies between 3.8 ( $t = 100$  s)

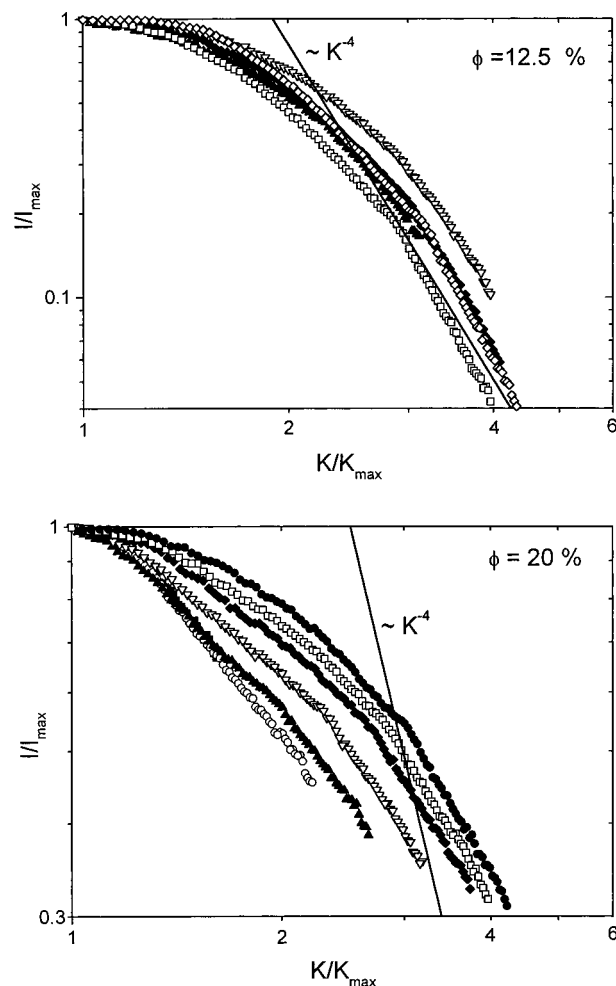


**Figure 8.** Same data as given in Figure 7 in a log-log representation. The solid line represents a  $K^{-4}$  dependence.

and 4.6 ( $t = 660$  s) with increasing time, whereas at 20%  $\beta$  increases from 1.2 ( $t = 10$  s) to 1.5 ( $t = 60$  s). The data indicate that in the 12.5% dispersion, sharp interfaces have already developed after 100 s, contrary to the 20% system; 60 s after homogenization,  $\beta$  is still small here. The fact that for 12.5% an exponent around 4 is found complements the microscopy observations where indeed discrete droplets become visible after 10 min. A direct comparison with microscopy for the 20% sample cannot be made because under the polarization microscope the first clear changes become visible only after 5 min. At this time the SALS ring has already collapsed.

From the SALS data and the microscopy observations it is concluded that the spinodal point in this system is situated close to  $\phi_I$ , contrary to Onsager's theory, which predicts this point to be close to  $\phi_N$ . There is evidence that polydispersity does shift the position of the spinodal point to relatively lower volume fractions. Vroege and Lekkerkerker<sup>30</sup> found that in the case of a polydisperse system (in length), the rescaled volume fraction  $(\langle L \rangle_w / D)\phi$  with  $\langle L \rangle_w$  the weight-averaged length of the rods has a value of 4 at the spinodal point. With respect to this rescaled concentration polydispersity gives rise to the formation of more concentrated nematics compared to the coexisting isotropic phase, which explains the shift of the spinodal point to relatively lower concentrations.

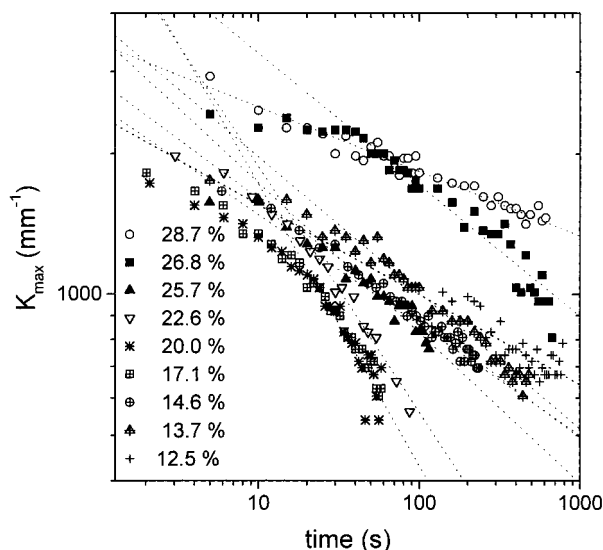


**Figure 9.** Time evolution of  $K_{\max}$  for concentrations ranging from  $\phi_1$  to  $\phi_N$  in log–log representation. The dotted lines are fits through the tails of the curves.

**4.2. Kinetics.** The crystallization kinetics in dispersions of spherical colloidal particles has been investigated by several authors by probing the position, the intensity and the width of the (111) Bragg peak<sup>25,26</sup> as a function of time or by means of SALS.<sup>24</sup> A nematic does not exhibit Bragg reflections due to fluidlike positional order, so that only SALS experiments are meaningful. The progress of phase separation can be studied by determining the growth exponent  $\alpha$  with which  $K_{\max}$  decreases in time

$$K_{\max} \sim t^{-\alpha} \quad (4.4)$$

where  $t$  is the time and  $\alpha$  is the decay exponent. This relationship is predicted to hold for both nucleation-and-growth and spinodal decomposition. For a spinodal process the following time evolution of  $\alpha$  is expected. In the initial stage the light scattering ring grows at fixed angle.<sup>31</sup> So in the initial stage,  $\alpha = 0$ . From our data, it is clear that the initial regime is never seen: as soon as a scattering peak is detected, it is shifting. In the intermediate stage Dhont showed that for spinodal decomposition in a system of spherical particles  $\alpha$  depends on both the quench depth as well as the significance of hydrodynamic interactions.<sup>27</sup> It is found that hydrodynamic interactions increase  $\alpha$ , where the value of  $\alpha$  is between 0.2 and 1.1. For a phase transition with a nonconserved order parameter, as in the case of the isotropic–nematic phase transition, the thermodynamic driving force of phase separation will be larger when the concentration of the metastable isotropic phase is larger. So at *higher* “supersaturation”, enhanced hydrodynamic interactions and a stronger thermodynamic driving force both lead to an *increase* of  $\alpha$ . In the late stage of spinodal decomposition and in the case of nucleation-and-growth, separate droplets are formed and growth can occur either by coalescence<sup>32</sup> or Ostwald ripening.<sup>33</sup> For both processes  $\alpha = 1/3$  is predicted.<sup>32,33</sup> In Figure 9 the shift of  $K_{\max}$  as a function of time is given in a log–log representation. Whereas initially eq 4.4 does not describe the time dependence of  $K_{\max}$ , it does apply for longer times. Moreover a strong

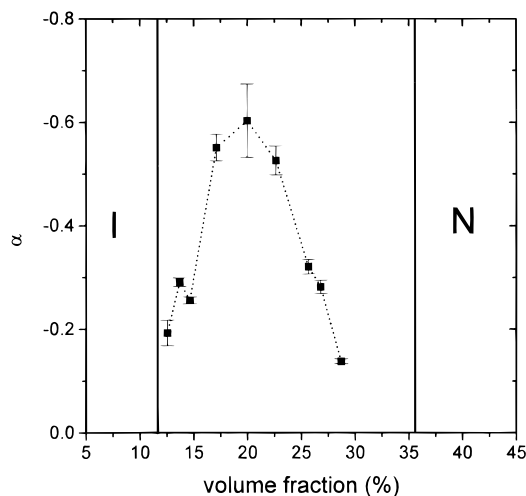


**Figure 10.** Concentration dependence of the slope of  $\log(K_{\max})$  vs  $\log(t)$  at  $500 \text{ mm}^{-1} \leq K_{\max} \leq 1000 \text{ mm}^{-1}$ , as obtained from the fits shown in Figure 9.

dependence of  $\alpha$  on concentration is observed. As can be seen from Figure 9, the slopes  $\alpha$  do not correspond to the same *times* but rather to the same range of  $K_{\max}$ -values. So  $\alpha$  gives the growth rate of  $K_{\max}$ -values between  $500 \text{ mm}^{-1}$  and  $1000 \text{ mm}^{-1}$ . Since the dominant length scale  $\Lambda_{\max}$  and the scattering vector  $K_{\max}$  are related by

$$\Lambda_{\max} = \frac{2\pi}{K_{\max}} \quad (4.5)$$

this range of  $K$ 's corresponds to  $\Lambda$ 's between 6 and 13  $\mu\text{m}$ . The concentration dependence of  $\alpha$  is given in Figure 10. Up to 15%,  $\alpha$  has a value between 0.2 and 0.3 and increases for higher concentrations as might be expected from the above given analysis. However, a maximum is reached at 20%, above which  $\alpha$  decreases again. The occurrence of the pronounced maximum is not expected from thermodynamics but instead has to do with the slowing down of the dynamics in the dispersions at higher concentration.

Another manner to study phase-separation kinetics is by monitoring the turbidity of the dispersion during phase separation. The *initial* rate of phase separation  $v_{\text{init}}$  can be defined as the increase of the turbidity  $\tau_0$  at  $t = 0$  s, normalized on the turbidity  $\tau_0$  at  $t = 0$  s:

$$v_{\text{init}} = \tau_0^{-1} \left( \frac{d\tau}{dt} \right)_{t=0} \quad (4.6)$$

This quantity is a measure for the *initial* rate with which density inhomogeneities develop in the metastable or unstable system. The kinetic picture that arises in this way is shown in Figure 11. Again a pronounced maximum is found at about 20%, which is at one-third of the coexistence region. Apparently the initial rate of phase separation as well as the rate of phase separation corresponding to later stages are at a maximum at this concentration.

Finally the value of the dominant length scale  $\Lambda_{\max}$  after 100 s was determined by interpolating the fits of the tails in Figure 9 to  $t = 100$  s. The dominant length scale determined in this way is shown as a function of concentration in Figure 12. Again at 20% a maximum is observed where the dominant length scale is 15  $\mu\text{m}$ . One might argue that the larger the dominant length

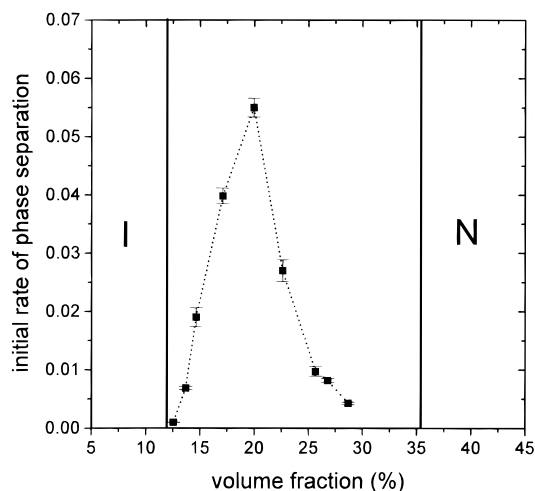


**Figure 11.** Increase of the normalized turbidity at  $t = 0$ s which is a measure for the initial rate of phase separation, as a function of the overall rod volume fraction.

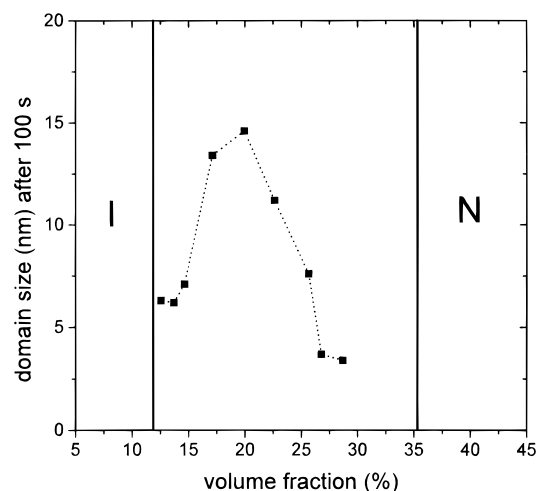


**Figure 12.** Domain size as a function of the overall volume fraction, 100 s after homogenization.

scale in the system, the further the phase separation process has developed. However, one should be careful with this since it is known that the dominant length scale in the initial stage, i.e., the *linear* Cahn regime,<sup>31</sup> depends on the quench depth. The deeper the quench, the smaller the dominant length scale.<sup>8</sup> Since the growth exponent  $\alpha$  of  $K_{\max}$  has a maximum at 20% (Figure 10), it is indeed expected that at later stages of the phase separation process the dominant domain size in samples with a concentration higher than 20% decreases with the concentration. Because below 20%, the dominant length scale at  $t = 100$  s decreases with concentration, we conclude that the decrease of phase separation kinetics is prevailing here.

## 5. Conclusions

Polarization microscopy shows that at a volume fraction of 12.5%, which is close to  $\phi_I$ , phase separation takes place by the formation of nematic droplets which appear within minutes after homogenization of the sample. The SALS scattering curves taken after a few minutes after homogenization obey  $K^{-\beta}$  behavior with  $\beta = 4$ , indicating that sharp interfaces are present in the system. Above a volume fraction of 20% phase separation proceeds by the formation of an initially interconnected structure which roughens in time, and

only at much later times, isolated droplets are formed. In this dispersion,  $\beta$  is much smaller than 4 at earlier times, revealing that within the time lapse of the SALS measurement no sharp interfaces have yet been formed at this concentration. The phenomena at 20% clearly resemble spinodal decomposition. Although both mechanisms eventually lead to separate droplets, the fact that at 12.5% the rate of phase separation is found to be significantly lower than at 20% indicates that droplet formation at 12.5% must be due to another mechanism than spinodal decomposition.

The crossover from nucleation and growth to spinodal decomposition is not as deep in the two-phase region as is expected from the Onsager theory. In fact the spinodal point is very close to the volume fraction  $\phi_I$ , where the isotropic phase becomes unstable, whereas Onsager theory predicts a spinodal point which is close to  $\phi_N$ . It is however noted that in this theory monodispersity, infinite aspect ratios, and true hard interactions are assumed. Although the experimental system is prepared with the intention to serve as model system, the rods aspect ratio is finite, the dispersion is not monodisperse, and any sterically stabilized dispersion is not perfectly hard. It is obvious that these experimental deviations from the presumptions in Onsager's theory will alter the position of the spinodal point.

The appearance of an optimum concentration at which phase separation is maximal is thought to be the result of the competition between the thermodynamic driving force which becomes larger at higher concentrations and particle dynamics which slows down. An optimum concentration at which crystallization kinetics is maximal is also found for the nucleation of hard and Yukawa colloidal spheres.<sup>25,26</sup> A striking difference however is that the maximum crystallization rate is found at the *melting* volume fraction, whereas here it is closer to the *freezing* volume fraction  $\phi_I$ . The underlying reason for this difference might be that the dynamics for rods depend stronger on concentration than for spherical particles. Evidence for this assumption is found in recently published results on long-time self-diffusion in dispersions of nearly hard colloidal rods.<sup>34</sup>

**Acknowledgment.** Liesbeth Donselaar and Johan Buitenhuis are thanked for preparing and characterizing the sterically stabilized boehmite dispersion, Felix van der Kooij for performing the rheology measurements, and Carel van der Werf for upgrading the SALS software. This work was supported by The Netherlands Foundation for Chemical research (SON) with financial aid from the Netherlands Organization for Scientific Research (NWO).

## References and Notes

- (1) Onsager, L. *Ann. N.Y. Acad. Sci.* **1949**, *51*, 627.
- (2) Shimada, T.; Doi, M.; Okano, K. *J. Chem. Phys.* **1988**, *88*, 7181.
- (3) Zocher, H. *Z. Anorg. Chem.* **1925**, *147*, 91.
- (4) Bowden, F. C.; Pirie, N. W.; Bernal, J. D.; Frankuchen, I. *Nature* **1936**, *138*, 1051.
- (5) Zocher, H.; Török, C. *Kolloid Z.* **1960**, *170*, 140.
- (6) Nakai, A.; Shiwaku, T.; Hasegawa, H.; Hashimoto, T. *Macromolecules* **1986**, *19*, 3008.
- (7) Nakai, A.; Shiwaku, T.; Hasegawa, H.; Hashimoto, T. *Macromolecules* **1996**, *29*, 5990.
- (8) Dorgan, J. R.; Yan, D. *Macromolecules* **1998**, *31*, 193.
- (9) Chowdhury, A. H.; Russo, P. S. *J. Chem. Phys.* **1990**, *92*, 5744.

- (10) Buining, P. A.; Pathmamanoharan, C.; Jansen, J. B. H.; Lekkerkerker, H. N. W. *J. Am. Ceram. Soc.* **1991**, *74*, 1303.
- (11) Buining, P. A.; Veldhuizen, Y. S. J.; Pathmamanoharan, C.; Lekkerkerker, H. N. W. *Colloids Surf.* **1992**, *64*, 47.
- (12) van Bruggen, M. P. B. *Langmuir* **1998**, *14*, 2245.
- (13) Buitenhuis, J.; Donselaar, L. N.; Buining, P. A.; Stroobants, A.; Lekkerkerker, H. N. W. *J. Colloid Interface Sci.* **1995**, *175*, 46.
- (14) Brenner, H. *Int. J. Multiphase Flow* **1974**, *1*, 195.
- (15) Berry, D. H.; Russel, W. B. *J. Fluid Mech.* **1987**, *180*, 475.
- (16) Wierenga, A. M.; Philipse, A. P.; Lekkerkerker, H. N. W.; Boger, D. V. *Langmuir* **1998**, *14*, 55.
- (17) Bolhuis, P. G.; Frenkel, D. *J. Chem. Phys.* **1997**, *107*, 1551.
- (18) Lekkerkerker, H. N. W.; Coulon, Ph.; van der Haegen, R.; Deblieck, R. *J. Chem. Phys.* **1984**, *80*, 3425.
- (19) Vroege, G. J.; Lekkerkerker, H. N. W. *J. Phys. Chem.* **1993**, *97*, 3601.
- (20) Buining, P. A.; Lekkerkerker, H. N. W. *J. Phys. Chem.* **1993**, *97*, 11510.
- (21) Schätzel, K.; Ackerson, B. J. *Phys. Rev. E* **1993**, *48*, 3766.
- (22) Verhaegh, N. A. M.; van Duijneveldt, J. S.; Dhont, J. K. G.; Lekkerkerker, H. N. W. *Physica A* **1996**, *230*, 409.
- (23) Binder, K. *Phase Transformations of Materials*; Materials Science and Technology 5; VCH Verlag: Weinheim, Germany 1991.
- (24) Schätzel, K.; Ackerson, B. J. *Phys. Rev. Lett.* **1992**, *68*, 337.
- (25) Harland, J. L.; van Meegen, W. *Phys. Rev. E* **1997**, *55*, 3054.
- (26) Dhont, J. K. G.; Smits, C.; Lekkerkerker, H. N. W. *J. Colloid Interface Sci.* **1992**, *152*.
- (27) Dhont, J. K. G. *J. Chem. Phys.* **1996**, *105*, 5112.
- (28) Furukawa, H. *Physica A* **1984**, *123*, 497.
- (29) Porod, G. *Small-angle X-ray scattering*; (Academic Press: London, 1982).
- (30) Vroege, G. J.; Lekkerkerker, H. N. W. *Rep. Prog. Phys.* **1992**, *55*, 1093.
- (31) Cahn, J. W. *Trans. Metall. Soc. AIME* **1968**, *242*, 166.
- (32) Binder, K.; Stauffer, D. *Phys. Rev. Lett.* **1974**, *33*, 1006.
- (33) Lifshitz, I. M.; Slyosov, V. V. *J. Phys. Chem Solids* **1961**, *19*, 35.
- (34) van Bruggen, M. P. B.; Lekkerkerker, H. N. W.; Dhont, J. K. G. *Phys. Rev. E* **1997**, *56*, 4394.

MA981196E